applied sciences

MDPI

Article

Topology Optimization of Hydrodynamic Body Shape for Drag Reduction in Low Reynolds Number Based on Variable Density Method

Ning Zhao [1,2], Jianyu Zhang [1], Haitao Han [1], Yongzhuang Miao [1,2] and Yongbo Deng [1,*]

[1] Changchun Institute of Optics, Fine Mechanics and Physics (CIOMP), Chinese Academy of Sciences, Changchun 130033, China; zn970123@163.com (N.Z.)
[2] University of Chinese Academy of Sciences, Beijing 100000, China
* Correspondence: dengyb@ciomp.ac.cn

Featured Application: The developed topology optimization approach may give a potential design idea for body shape drag reduction of micro underwater vehicles and other underwater equipment worked in low speed.

Abstract: This paper presents a variable density topology optimization method to numerically investigate the optimal drag-reduction shape of objects in the two-dimensional and three-dimensional flows with steady incompressible external flow conditions, taking into account material volume constraints. By introducing the porous media model, the artificial Darcy friction is added to the Navier-Stokes equation to characterize the influence of materials on the fluid. Material density is applied to implement material interpolation. By transforming the boundary integral form of viscous dissipative expression of drag into the volume integral of artificial Darcy friction and convection term, we solve the problem of drag expression on the implicit interface corresponding to the structure. The continuous adjoint method is used to analyze gradient information for iteratively solving topology optimization problems. We obtain the relevant topology optimization structures of the minimum drag shapes, investigate the effect of the low Reynolds number on the drag force corresponding to two objective functions and discuss the mechanism of drag reduction by a hydrodynamic body shape.

Keywords: variable density method; topology optimization; drag reduction; porous medium model; adjoint analysis

Citation: Zhao, N.; Zhang, J.; Han, H.; Miao, Y.; Deng, Y. Topology Optimization of Hydrodynamic Body Shape for Drag Reduction in Low Reynolds Number Based on Variable Density Method. *Appl. Sci.* **2023**, *13*, 5461. https://doi.org/10.3390/app13095461

Academic Editor: Maria Grazia De Giorgi

Received: 27 February 2023
Revised: 15 April 2023
Accepted: 21 April 2023
Published: 27 April 2023

1. Introduction

Drag reduction has long been noticed and studied as an important way to achieve long voyage goals and energy-saving requirements in marine strategies [1]. Especially for micro underwater vehicles with small size and less power sources, it is more important to reduce energy consumption. There are active methods for drag reduction, which require additional energy consumption, such as reverse jet [2] and cavitation [3], and passive methods such as groove structures [4] and hydrophobic surfaces [5]. At the beginning of the above optimization methods, the optimal design of a hydrodynamic body shape is a rather important antecedent in the drag-reduction step of underwater vehicles, and a good streamlined body shape contributes a large percentage to the drag reduction.

Current research on underwater body shape for drag reduction mainly focuses on the parametric optimization using simplified models or constructing alternative models [6–12]. The vast majority of them are shape optimization of existing models, which are empirical, intuitive and not optimal results in a certain range of operating conditions. In order to obtain the optimal flexible choice for different design objectives in different flow field conditions, we introduce the variable density method to realize the topology optimization of the body shape.

Topology optimization is a powerful method for the structural inverse design, which generates structures that meet the optimization objectives directly in the design domain through a holistic mathematical approach [13]. Compared with the shape optimization and the dimensional optimization, topology optimization has a greater design freedom and requires low priori for defining the initial structure. In addition, topology optimization can also ensure the manufacturability of the generated structures by using additional constraints [14,15]. Its concept originates in the field of solid mechanics and first appeared in the design of truss structures [16]. Since Bendsøe and Kikuchi [17] pioneered the homogenization method to describe structural topology in terms of material distribution in 1988, various topology optimization methods, such as the asymptotic structure optimization method [18], the variable density methods [19] and the level set method [20], have been widely used in multiple research fields, such as acoustics, optics, electronics, heat conduction, fluid flow and combined applications of multiphysics disciplines [21–26].

The problem of the optimal body shape can be traced back to Pironeau's research [27] on the minimum drag in Stokes flow. Later on, some problems on drag and lift were studied [28–32]. Reference [29] studies the drag and lift of the 2D time-dependent flow around a cylinder. As the fluid stream passes the topmost part of the cylinder, it tends to separate from the top surface and peel off in a clockwise motion as it approaches the rear end of the cylinder, ending up as a shed vortex which can be quantified [33] and represents a dangerous structural problem [34]. In relevant fluid dynamics problems, uncertainty quantification is often used to introduce the uncertainty into a mathematical and physical model to make it more realistic [35,36]. In the topology optimization of fluid, Borrvall and Peterson [37] develop a porous media model for the Stokes flow, which was soon extended to the Navier-Stokes flow [38,39]. In this model, porous media is filled in the two-dimensional(2D) or three-dimensional(3D) design domain, and the artificial Darcy friction is added to the Stokes equation and the Navier-Stokes equation to characterize the effect of the material on the fluid. [40] gives a detailed introduction to density-based topology optimization of fluid flow problems with implementation in MATLAB. Compared with [38,39], we extend topology optimization to 3D external flow problems. In this paper, porous media is filled in a steady incompressible fluid, and material density is applied for implementing material interpolation. Meanwhile, the finite element method is used to solve the governing equations; the adjoint sensitivity is analyzed by the continuous adjoint method to update the design variable and iteratively evolve the fluid structure. The objective function takes the volume integral form of the drag expression to solve external flow problems. The variable density topology optimization model of Navier-Stokes flow is established to study the 2D and 3D body shape for drag reduction.

The rest of the article is as follows. The second section presents the overall description of the topology optimization problem using the variable density method for the steady incompressible flows. The third section covers specific operational details of the numerical solution. The fourth section presents specific numerical examples in two and three dimensions. The fifth section provides the relevant conclusions.

2. Methodology

In this section, we use the material distribution method to construct the topology optimization model for steady incompressible fluids.

2.1. Governing Equations

We seek the optimum body shapes in the flow. To achieve that, we first introduce $\gamma \in \{0, 1\}$ as the design variable, which is a binary distribution defined in the design domain. Respectively, 0 and 1 represent the solid phase and liquid phase, corresponding to the presence or absence of material at an arbitrary point within the design domain. In this problem, the distribution of the solid material is the optimal body structure we expect to obtain within the flow field, so the essence of the topology optimization is an optimization problem with 0–1 discrete variables. In order to adopt an optimization algorithm based on

continuous variables and avoid the difficulties of solving binary optimization problems, we can relax γ to [0, 1] to achieve continuous variation. Figure 1 is a schematic representation of the fluid topology optimization problem. The shape optimization problem is defined in a bounded domain Ω. Ω is the fluid domain and Ω_S is the design domain; both of them are separated by the boundary Γ_S.

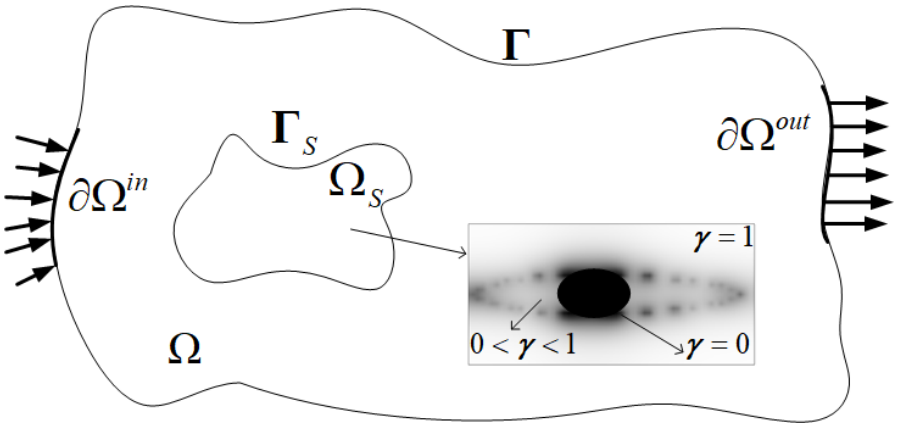

Figure 1. Schematic of the fluid flow problem.

The above model in a steady incompressible laminar flow (ignoring gravity effect) can be described by the stationary incompressible Navier-Stokes equation with boundary conditions as:

$$\begin{cases} \rho\mathbf{u}\cdot\nabla\mathbf{u}+\nabla\cdot\left[-\mu(\nabla\mathbf{u}+\nabla^T\mathbf{u})+p\mathbf{I}\right]=\mathbf{f} & \text{in } \Omega \\ -\nabla\cdot\mathbf{u}=0 & \text{in } \Omega \\ \mathbf{u}=\mathrm{u}_0 & \text{on } \partial\Omega^{in} \\ \left[-\mu(\nabla\mathbf{u}+\nabla^T\mathbf{u})+p\mathbf{I}\right]\cdot\mathbf{n}=0 & \text{on } \partial\Omega^{out} \\ \mathbf{u}=0 & \text{on } \Gamma_s \\ \mathbf{u}\cdot\mathbf{n}=0 & \text{on } \Gamma \end{cases} \tag{1}$$

where ρ is the fluid density, μ is the viscosity, $\mathbf{I}$ is the unit tensor, $\mathbf{f}$ is the body force vector (source term), and $\mathbf{n}$ is the unit outward normal vector on the boundary of flow domain. The fluid velocity vector $\mathbf{u}$ and pressure p, which characterize the fundamental motion of the particles in the flow field, are the only solutions to the system (1).

In order to solve the Navier-Stokes equation, boundary conditions are necessary to set in Equation (1), where the normal stress at the outlet boundary $\partial\Omega^{out}$ is zero; initial velocity at the inlet boundary $\partial\Omega^{in}$ is a constant u_0; the velocity at the fluid-solid interface Γ_s is zero; and $\Gamma=\partial\Omega\backslash\left(\partial\Omega^{in}\cup\partial\Omega^{out}\right)$ denotes the free-slip boundaries.

To facilitate the calculation, we introduce the reference length L and the reference velocity U to make all variables in a dimensionless form as:

$$\mathbf{u}=\frac{\mathbf{u}}{U},\ p=\frac{pL}{\mu U},\ \mathbf{f}=\frac{\mathbf{f}L^2}{\mu U},\ \nabla=L\nabla\ \ \mathrm{Re}\equiv\frac{\rho LU}{\mu} \tag{2}$$

where Re is the Reynolds number defined as the ratio of the inertial force to the viscous force. The dimensionless momentum equation is as follows:

$$\mathrm{Re}\mathbf{u}\cdot\nabla\mathbf{u}+\nabla\cdot\left[-(\nabla\mathbf{u}+\nabla^T\mathbf{u})+p\mathbf{I}\right]=\mathbf{f}\ \text{in}\ \Omega \tag{3}$$

For using adjoint analysis later, we give a variational description of Navier-Stokes equations as follows:

$$\begin{aligned}&\text{Find}\begin{cases}\mathbf{u}\in\mathcal{L}^2(\Omega)\text{ with }\begin{cases}\mathbf{u}=\mathbf{u}_0 & \text{on }\partial\Omega^{in}\\ \mathbf{u}\cdot\mathbf{n}=0\text{ on }\Gamma\end{cases}\\ p\in\mathcal{L}^2(\Omega)\text{ with }p=p_0\text{ on }\partial\Omega^{out}\end{cases}\\ &\int_\Omega \mathrm{Re}(\mathbf{u}\cdot\nabla\mathbf{u})\cdot\tilde{\mathbf{u}}+(\nabla\mathbf{u}+\nabla^T\mathbf{u}):(\nabla\tilde{\mathbf{u}}+\nabla^T\tilde{\mathbf{u}})-p\nabla\cdot\tilde{\mathbf{u}}+\mathbf{u}\cdot\nabla\tilde{p}-\mathbf{f}\cdot\tilde{\mathbf{u}}\,\mathrm{d}\Omega=0\\ &\text{for }\forall\tilde{\mathbf{u}}\in\mathcal{H}(\Omega)\text{ and }\tilde{p}\in\mathcal{H}(\Omega)\end{aligned}\tag{4}$$

where $\mathcal{H}(\Omega)$ represents the first order Hilbert spaces defined in Ω, and $\mathcal{L}^2(\Omega)$ represents the second order Lebesgue spaces defined in Ω.

2.2. Material Interpolation

The governing equations for nonhomogeneous materials can be obtained by introducing a source term to the Navier-Stokes equation. The effect of the material distribution on the fluid motion is modeled with the penalty parameter [37]. Here, we use a porous medium model and introduce a dimensionless artificial Darcy friction force in the momentum equation to act as a source term, which is assumed to be proportional to the velocity defined as:

$$\mathbf{f}=-\alpha\mathbf{u}\text{ in }\Omega_s\tag{5}$$

where α is the material impermeability which represents the ability to transport liquid. It can be expressed as:

$$\alpha=\begin{cases}+\infty\text{ for }\gamma_p=0\\ 0\quad\text{for }\gamma_p=1\end{cases}\tag{6}$$

where γ_p is the material density obtained by successively implementing filtering and thresholding projection operations on the design variable γ taking consecutive values in [0, 1]. For avoiding problems such as gray scale, the design variable is regularized by Helmholtz filters in variable density topology optimization problems [41] as follows:

$$\begin{aligned}\nabla\cdot(-r_f^2\nabla\gamma_f)+\gamma_f=\gamma &\quad\text{in }\Omega_s\\ r_f^2\nabla\gamma_f\cdot\mathbf{n}=0 &\quad\text{on }\Gamma_s\end{aligned}\tag{7}$$

where γ_f is the filtered design variable and r_f is the filter radius. The variational formulation of the PDE filter defined in Ω_s can be derived as:

$$\begin{aligned}&\text{Find }\gamma_f\in\mathcal{H}(\Omega)\,for\,\gamma\in\mathcal{L}^2(\Omega)\\ &\int_\Omega r_f^2\nabla\gamma_f\cdot\nabla\widetilde{\gamma}_f+\gamma_f\widetilde{\gamma}_f-\gamma\widetilde{\gamma}_f d\Omega=0\\ &\text{for }\forall\widetilde{\gamma}_f\in\mathcal{H}(\Omega)\end{aligned}\tag{8}$$

where $\widetilde{\gamma}_f$ is the test function of γ_f. Filtering produces a significant gray scale, which can be reduced by imposing a smooth step function called projection in topology optimization. The threshold projection of the filtered design variable based on the hyperbolic tangent function is [42]:

$$\gamma_p=\frac{\tanh(\beta\xi)+\tanh\Big(\beta\Big(\gamma_f-\xi\Big)\Big)}{\tanh(\beta\xi)+\tanh(\beta(1-\xi))}\tag{9}$$

where β and ξ are the parameters of projection slope and projection point, respectively [43]. In order to distinguish the solid phase from the liquid phase, the material interpolation of impermeability can be implemented as:

$$\alpha=\alpha_{\min}+(\alpha_{\max}-\alpha_{\min})q\frac{1-\gamma_p}{q+\gamma_p}\tag{10}$$

where q is the parameter for adjusting projection convexity and $\alpha_{\max}$ and $\alpha_{\min}$ are the impermeability of the solid and fluid phases, respectively. In theory, $\alpha_{\max}$ is the infinite value while $\alpha_{\min}$ is the infinitesimal value or zero, which is to ensure the stability of the numerical implementation and approximate the solid phase with enough accuracy [44].

2.3. Topology Optimization Problem

For the optimal drag reduction problem of body shape in the design domain, we have introduced the Naver-Stokes equation and the porous media model, and implement the material interpolation by the material density. Furthermore, to ensure the uniqueness of the solution, we add material volume and fixed-point constraints. Thus, the fluid topology optimization problem is described as:

$$\begin{aligned}
&\text{Find } \gamma : \Omega_s \to [0,1] \text{ to minimize } \tfrac{J}{J_0} \text{ with} \\
&J = \textstyle\int_\Omega A(\mathbf{u}, \nabla\mathbf{u}, p; \gamma_p)\mathrm{d}\Omega + \int_{\partial\Omega} B(\mathbf{u}, \nabla\mathbf{u}, p; \gamma_p)\mathrm{d}\Gamma \\
&\text{constrained by :} \begin{cases}
\left.\begin{cases} \mathrm{Re}\mathbf{u}\cdot\nabla\mathbf{u} + \nabla\cdot\left[-(\nabla\mathbf{u} + \nabla^T\mathbf{u}) + p\mathbf{I}\right] = \mathbf{f} \\ -\nabla\cdot\mathbf{u} = 0 \\ \mathbf{u}\cdot\mathbf{n} = 0 \end{cases}\right\} \text{in } \Omega \\
\alpha = \alpha_{\min} + (\alpha_{\max} - \alpha_{\min}) q \frac{1-\gamma_p}{q+\gamma_p} \\
\begin{cases} \nabla\cdot(-r_f^2\nabla\gamma_f) + \gamma_f = \gamma \text{ in } \Omega_s \\ r_f^2\nabla\gamma_f\cdot\mathbf{n} = 0 \qquad\qquad \text{on } \Gamma_s \end{cases} \\
\gamma_p = \frac{\tanh(\beta\xi) + \tanh\left(\beta\left(\gamma_f - \xi\right)\right)}{\tanh(\beta\xi) + \tanh(\beta(1-\xi))} \\
|v - v_0| \le 10^{-5} \text{ with } v = \frac{1}{|\Omega|}\int_\Omega \gamma_p \mathrm{d}\Omega
\end{cases}
\end{aligned} \tag{11}$$

where J represents the design objective and J_0 represents its value of the first iterative solution. v is the area fraction which represents the proportion of fluid in the design domain and $v_0 \in (0, 1)$ is its set value; $|\Omega| = \int_\Omega 1 \, \mathrm{d}\Omega$ is the volume of Ω_s.

2.4. Adjoint Analysis

Previously, we have mentioned the control equations describing the physical field distribution and the constraint equations on the variables. To avoid the use of direct solutions, this topology optimization problem, which is a nonlinear set of partial differential equations, can be solved by using an iterative process based on gradient information determined by the adjoint sensitivity. The sensitivity of J is obtained by adjoint analysis [45] below:

$$\delta J = -\int_\Omega \gamma_{fa}\, \delta\gamma \mathrm{d}\Omega \tag{12}$$

where δ is the operator for the first order variational of a variable; $\delta\gamma \in \mathcal{L}^2(\Omega)$ is the first order variational of γ; and γ_{fa} is the adjoint variable of the filtered design variable γ_f. The adjoint form of Naiver-Stokes equations is as:

$$\begin{aligned}
&\textstyle\int_\Omega \frac{\partial A}{\partial \mathbf{u}}\cdot\tilde{\mathbf{u}}_a + \frac{\partial A}{\partial \nabla\mathbf{u}} : \nabla\tilde{\mathbf{u}}_a + \frac{\partial A}{\partial p}\tilde{p}_a - \mathrm{Re}(-\mathbf{u}\cdot\nabla\mathbf{u}_a + \mathbf{u}_a\cdot\nabla^T\mathbf{u})\cdot\tilde{\mathbf{u}}_a + \\
&(\nabla\mathbf{u}_a + \nabla^T\mathbf{u}_a) : (\nabla\tilde{\mathbf{u}}_a + \nabla^T\tilde{\mathbf{u}}_a) + \mathbf{u}_a\cdot\nabla\tilde{p}_a - p_a\nabla\cdot\tilde{\mathbf{u}}_a + \alpha\mathbf{u}_a\cdot\tilde{\mathbf{u}}_a \, \mathrm{d}\Omega = 0
\end{aligned} \tag{13}$$

where $\mathbf{u}_a \in \mathcal{H}(\Omega)$ and $p_a \in \mathcal{L}^2(\Omega)$ are the adjoint variables of $\mathbf{u}$ and p, respectively; and $\tilde{\mathbf{u}}_a \in \mathcal{H}(\Omega)$ and $\tilde{p}_a \in \mathcal{L}^2(\Omega)$ are the test functions of $\mathbf{u}_a$ and p_a, respectively. The adjoint form of the filter is:

$$\int_\Omega r_f^2\nabla\gamma_{fa}\cdot\nabla\tilde{\gamma}_{fa} + \gamma_{fa}\tilde{\gamma}_{fa} \, \mathrm{d}\Omega = 0 \tag{14}$$

where $\tilde{\gamma}_{fa} \in \mathcal{H}(\Omega)$ is the test function of $\gamma_{fa} \in \mathcal{H}(\Omega)$. The adjoint sensitivity of v is obtained as:

$$\delta v = -\frac{1}{|v|}\int_{\Omega} \gamma_{fa}\delta\gamma \, \mathrm{d}\Omega \tag{15}$$

where γ_{fa} can be derived from the following variational formulation for the adjoint equation of the PDE filter:

$$\int_{\Omega} \frac{\partial\gamma_p}{\partial\gamma_f}\widetilde{\gamma}_{fa} + r_f^2\nabla\gamma_{fa}\cdot\nabla\widetilde{\gamma}_{fa} + \gamma_{fa}\widetilde{\gamma}_{fa}\mathrm{d}\Omega = 0, \quad for\ \forall\widetilde{\gamma}_{fa} \in \mathcal{H}(\Omega) \tag{16}$$

2.5. Solution Procedures

The topology optimization problem for steady incompressible fluids has been outlined. After giving the initial conditions and the expression of the objective function for the specific drag force problem, it can be solved according to the following steps.

1. Assume an initial guess of the distribution of the design variable γ in Ω_S as the initial structure determined by the constraint of fixed point.
2. Solve the partial differential equations constraint with the current design variable.
3. Solve the adjoint equations based on the solution of the partial differential equations constraint.
4. Calculate the adjoint derivatives of the optimized objective function and update the distribution of γ by the method of moving asymptotes (MMA) according to the sensitivity.
5. Check the convergence criterion. If it is satisfied, the procedure is terminated; if not, the procedure will return to 2.

All the above procedures, including sensitivity analysis based on adjoint method and update iteration based on the method of moving asymptotic, were implemented through the secondary development of MATLAB code. Linear solutions were implemented on the finite element solver PARDISO based on COMSOL Multiphysics, while the Newton iteration method was used for nonlinear solutions.

3. Numerical Implementation

We have presented the problem of topology optimization in Equation (11). The pseudocode in Algorithm 1 shows the iterative solving process and contains a loop for the solution. The variational formulations of the partial differential equations and adjoint equations [45,46] are solved by finite element method [47]. The distribution of γ is updated by MMA [48].

The values of each parameter in topology optimization are set at the beginning of the procedure. In the process of solving, r_f is kept as 0.1; β with the initial value of 1 is doubled after every 30 iterations [49]. The maximum number of iterations is 315 and the corresponding value of β is 2^{10}. The greater the value of β is, the clearer the material interface is.

In the iterative solving loop, n_i and n_{max} are the loop index and its maximal value, respectively. J_{n_i} is the specific value of J in the n_i-th iteration, and mod is an operator for taking the remainder. The loop will stop at the maximal number of iterations. It also will terminate when both the average variation of J for five consecutive iterations and the residual of v are less than the tolerance of 10^{-5}.

Algorithm 1: Iterative solution of Equation (11). Pseudocode used to solve the topology optimization problem for the Navier-Stokes flows.

Set u_0 v_0 Re h η,

Set $\begin{cases} \gamma \leftarrow v_0 \\ n_i \leftarrow 1 \\ n_{\max} \leftarrow 315 \\ q \leftarrow 1 \end{cases}$ $\begin{cases} \alpha_{\min} \leftarrow 0 \\ \alpha_{\max} \leftarrow 10^4 \rho \\ \xi \leftarrow 0.5 \\ \beta \leftarrow 1 \end{cases}$

loop

Solve Equation (8) to derive γ_f by filtering γ;
Project γ_f to derive γ_p and compute v;
Solve **u** and p from Equation (4), and evaluate J/J_0;
Solve $\mathbf{u}_a$, p_a and γ_{fa} from Equations (13) and (14);
Evaluate δJ from Equation (12);
Solve γ_{fa} from Equation (16);
Evaluate δv from Equation (15);
Update γ based on δJ and δv;

if mod $(n_i, 30) == 0$
$\beta \leftarrow 2\beta$
end if

if $(n_i == n_{\max})$ or $\begin{cases} \beta = 2^{10} \\ 1/5 \sum_{m=0}^{4} |J_{n_i} - J_{n_i - m}| / J_0 \leq 10^{-5} \\ |v - v_0| \leq 10^{-5} \end{cases}$

break;
end if

$n_i \leftarrow n_i + 1$
end loop

4. Results and Discussion

In this section, we give numerical examples of 2D and 3D body shape topology optimization for drag reduction and the related results are obtained and discussed.

4.1. Two-Dimensional Examples

In the 2D drag minimization problem, the model is set up as shown in Figure 2, which is the visualization of the schematic Figure 1. The length and width of the flow domain Ω are 10L and 7L, respectively, and the length and width of the design domain Ω_s are 2L and L, respectively, with L = 1 (dimensionless). The fixed-point C is used to constrain the generation of solid material, and the structure generated in the first step of optimization is assumed to be the initial body shape. In order to solve the Navier-Stokes equation, the initial values of the boundaries are also needed as definite solution conditions. The far-field condition at the inlet $\partial\Omega^{in}$ and the boundary Γ is a uniform velocity in the X-direction of $u_0 = U = 1$ (dimensionless), and the constraint at the outlet $\partial\Omega^{out}$ is a normal stress $p = 0$ (dimensionless).

We consider the external flow with uniform velocity flowing around the isolated body. In this case, the fluidic drag is usually expressed as the boundary integral of the stress vector on the body surface, that is, the integral of the compressive stress and the viscous stress. However, because the shape of the topology optimization structure is unknown in advance, it is not applicable to this problem. In 2012, Kondoh put forward various objective function formulas for drag minimization and lift maximization, including the volume integral and area integral [50], through approximate transformation. In addition, the volume integration formula provides a better estimation of lift and drag coefficients than the conventional line integration along the streamline body; The volume integral formula is not sensitive to small changes in the mesh generated around the object [51]. Therefore, the objective function we use is in the form of the volume integral.

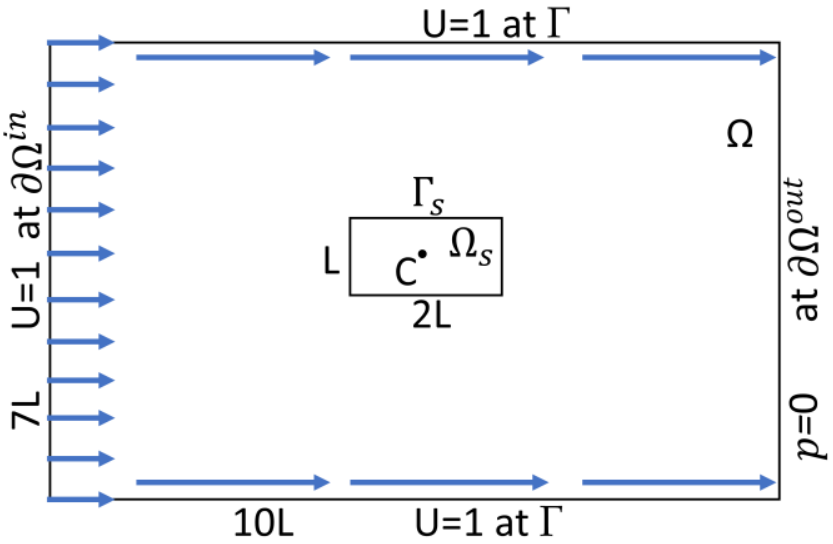

Figure 2. Settings for size and boundary conditions of two-dimensional (2D) model.

In the porous media model, the effect of solid material on the fluid is expressed as an artificial Darcy friction in the momentum equation, so the force **F** on the solid exerted by the fluid should be expressed as the volume integral of—**f** due to the action-reaction law. The expression of **F** can be defined as:

$$\mathbf{F} = -\int_{\Omega} \mathbf{f}\, d\Omega = \int_{\Omega} \alpha \mathbf{u}\, \mathrm{d}\Omega \tag{17}$$

Thus, fluid dynamic drag D can be expressed as the X-axis component of Equation (17) as:

$$J_1 = D = \int_{\Omega} \alpha \mathrm{u}\, \mathrm{d}\Omega \tag{18}$$

where u is the X-axis component of velocity vector **u** and J_1 is the objective function 1. Meanwhile, the existing drag formula through surface-stress integration is transformed by the Gaussian formula to the volume integral form as:

$$\begin{aligned} &\int_{\Gamma} \left[(\nabla \mathbf{u} + \nabla \mathbf{u}^T) - p\mathbf{I}\right] \mathbf{n}\, \mathrm{d}\Gamma = \int_{\Omega} \nabla \cdot \left[(\nabla \mathbf{u} + \nabla \mathbf{u}^T) - p\mathbf{I}\right] \mathrm{d}\Omega \\ &= \int_{\Omega} (\mathrm{Re}\mathbf{u} \cdot \nabla \mathbf{u} - \mathbf{f}) \mathrm{d}\Omega = \int_{\Omega} (\mathrm{Re}\mathbf{u} \cdot \nabla \mathbf{u} + \alpha \mathbf{u}) \mathrm{d}\Omega \end{aligned} \tag{19}$$

and the convection term is retained. Therefore, objective function 2 can be described as:

$$J_2 = \int_{\Omega} (\mathrm{Re}\mathbf{u} \cdot \nabla \mathbf{u} + \alpha \mathbf{u}) \mathbf{e}\, \mathrm{d}\Omega \tag{20}$$

where **e** is the unit vector in X-direction. Therefore, J_1 and J_2 are just different expressions of drag, with difference is with or without a convective term. J_2 is to characterize drag by adding the convective term on the basis of J_1.

4.1.1. Effect of Area Fractions for Design

In 2D problems of drag reduction, area fraction is an important constraint for structure solving, which represents the proportion of fluid structure in the design domain. Figure 3 shows that with the decrease of area fraction, the proportion of solid structure increases. Obviously, with the decrease of the proportion of solid materials, the resulting structures tend to be flat and slender. As a result, there is a problem with obtaining an incomplete structure within the design domain. Therefore, we can basically obtain the complete structure in the above 2D model with the area fraction of 0.8, when the Reynolds numbers are within 0–500. Of course, it is recommended to take a larger value.

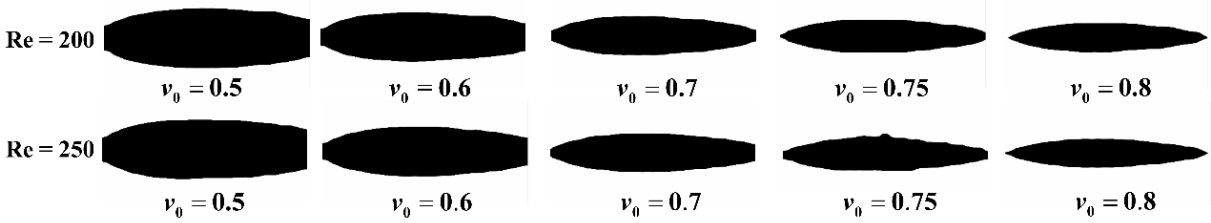

Figure 3. Structures of the different area fractions for Reynolds numbers (Re) of 200 and 250.

At the same time, drag values increase with the proportion of solid materials and the Reynolds number increases from Figure 4.

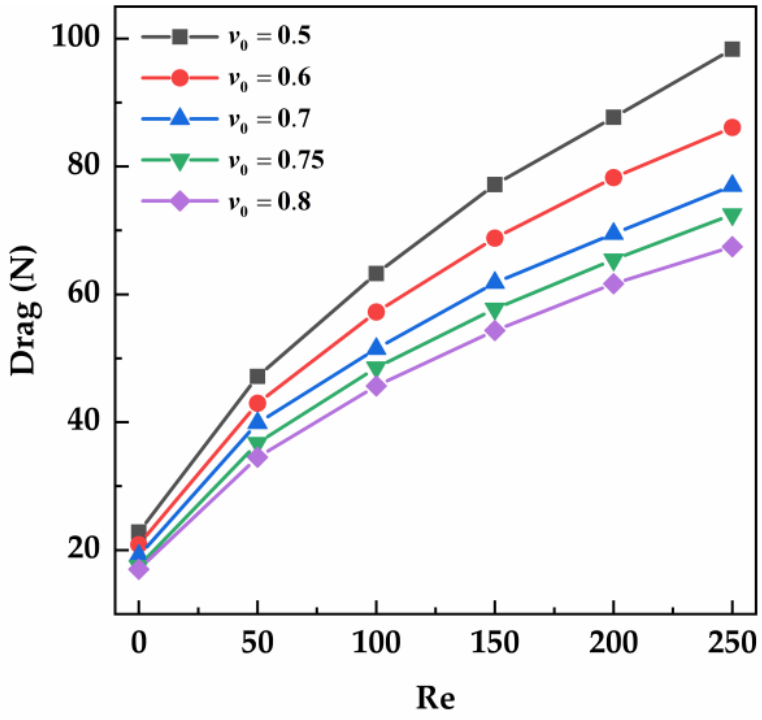

Figure 4. Drag values change with area fraction in different Reynolds numbers.

4.1.2. The Verification of Iterative Convergence

In addition to the value of area fraction, we also investigate the convergence of objective value and area constraint during the numerical computation to ensure the robustness and uniqueness of the solution. The accuracy of the area fraction is set to 10^{-5} and convergence performances of topology optimization for 2D drag reduction problem in laminar flow conditions are good. Figure 5 shows the convergence history and evolution curve of the iterative solution of the 2D model obtained by numerical computation with the Reynolds number of 200, the mesh density of 30, and the area fraction of 0.8. It can be observed that the initial topology is generated from the set central fixed point, and as the number of optimization iterations grows, the density projection gradually converges to 0 and 1 and the topology is gradually clear and complete. In fact, after the 180th iteration equivalent to $\beta \geq 2^6$, the objective value (0.3014) is basically unchanged and does not differ much from the result (0.2997) of the 315th iteration, but the density projection of the latter is closer to the 0–1 binary distribution and the results are clearer. Furthermore, the results show a convergence history with overall monotonicity and basically no local jumps caused by the projection operation. Therefore, the robustness of the numerical iterative solution can be confirmed and the structure is stable in the current setup conditions.

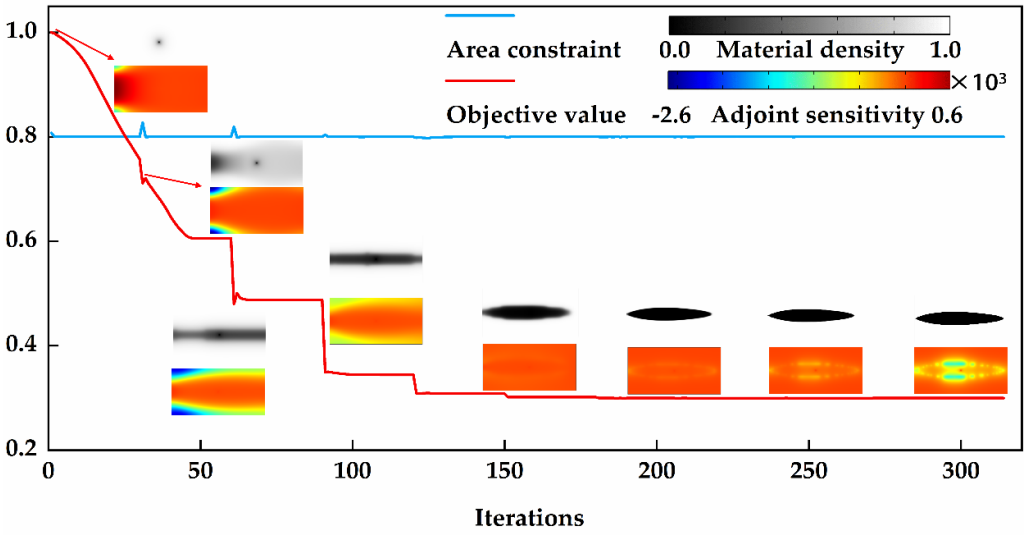

Figure 5. Convergent histories of the optimization objective and the area constraint, including the snapshots for the evolution of the material density and sensitivity distribution.

4.1.3. The Verification of Mesh Irrelevance

The calculation results rely on the custom filter radius and mesh density, and their relationship is defined as $r_f = h\eta$, where h is the mesh size as the reciprocal of the mesh density, and η is the length ratio parameter of the filter radius that we introduce. To maintain r_f unchanged, η changes with the variation of h. After numerical verification, η of 2–3 is appropriate for this problem. In order to verify the correlation between the obtained results and the mesh density, the mesh densities of 10, 30 and 60 are taken to calculate the drag values corresponding to different Reynolds numbers with the same other influencing factors. Table 1 shows the drag values of the 2D problem for each Reynolds number at different mesh densities when the area fraction is 0.8. The unit of drag is N. Although the mesh density has an effect on the flatness of the edges of the generated shape, it can be known that the effect error on the final drag value is less than 1%, which verifies that the result has very little dependence on mesh density within the appropriate range.

Table 1. Table of drag values for different mesh densities corresponding to various Reynolds numbers.

Re = 300	Mesh Size	Re = 0	Re = 1	Re = 20	Re = 50	Re = 100	Re = 150	Re = 200	Re = 250
$h = 1/10$	17.5045	17.5594	26.5496	36.7503	48.5749	57.7612	65.4489	72.4931	78.7289
$h = 1/30$	17.4802	17.4931	26.5447	36.8043	48.5007	57.6024	65.3731	72.2651	78.6652
$h = 1/60$	17.4328	17.4908	26.5356	36.7716	48.5069	57.5899	65.3632	72.2081	78.6638

4.1.4. Effect of Reynolds Numbers on Body Shapes and Drag Values

For 2D objects placed in uniform flow with velocity $u_0 = 1$ in X-direction, we investigate the profiles of objects with minimum drag. We employ the objective function J_1 and J_2, and apply the constraint that the area fraction of an object is a lower bound on the fluid structure in a 2D model. We also apply the constraint that the initial structure of the object is fixed at the origin so that the body location is anchored during the process of optimization.

The results of two different objective functions for drag minimization at various Reynolds numbers are presented in Figures 6 and 7. The overall optimized shape of the 2D model is nearly centered in the design domain with a shuttle shape. When the Reynolds number tends to zero, we express it as Re = 0 for convenience. Therefore, Re = 0 is the ideal state, which is an approximate simulation that expresses the ignorance of inertial forces. For the results with Re close to 1, they have basically the same shape profile. When the

Re is less than 200, the structure is nearly symmetrical up and down and the two sides of the mid-section are smooth. As the Reynolds number continues to increase, the profile grows laterally, the body shape gradually flattens, and the cone angles at both ends become smaller, while the lower edge changes more than the upper edge and the trailing section are relatively slender. The generated structures become so-called streamlined and have the tendency to go beyond the design domain. The above results are approximate to those obtained by Garcke using the phase field method with the different objective function [52].

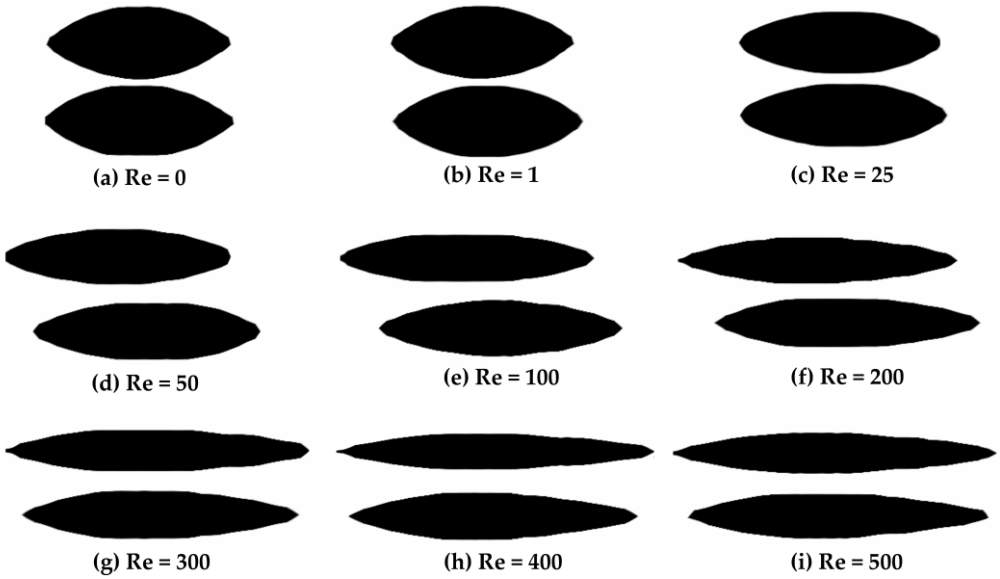

Figure 6. 2D optimal body shapes for drag reduction corresponding to two different objective functions at various Reynolds numbers. In the above illustrations from (**a**–**i**), the upper graph corresponds to J_1 and the lower one corresponds to J_2. The area fraction v_0 is set to 0.9 in both cases.

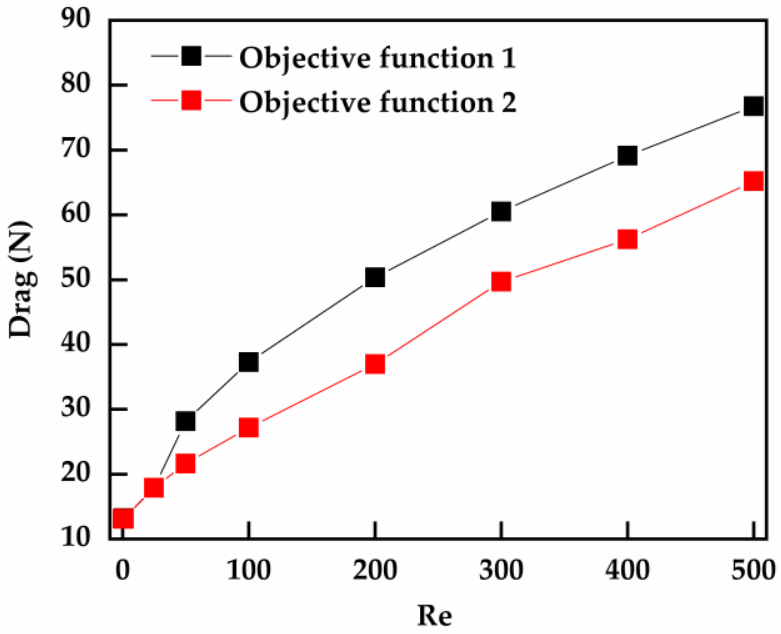

Figure 7. Comparison of the drag values for two objective functions at different Reynolds numbers in 2D problem. When the Reynolds number is less than 25, the red line partly overlaps and covers the black line.

Comparing the optimization results corresponding to objective functions 1 and 2 with the same area fraction of 0.9 in terms of the shape shown in Figure 6, the latter have a

smaller aspect ratio and the structures are all centered in the design domain; in terms of drag values shown from Figure 7, at Reynolds numbers less than 25, the drag values of both are approximate, and when greater than 50, the objective function with convection term corresponds to a smaller value. It means that as the Reynolds number increases, the effect of convection term on the drag values is also greater and should not be ignored.

Therefore, the results of J_1 and J_2 are not same. The reason for the difference is also caused by adding the convection term. Compared with J_1, J_2 corresponds to a result that is wider in shape and smaller in drag value. It is not that the smaller drag is necessarily better, but rather that the measurement criteria are different under different objective functions.

This paper uses the fixed mesh achieved by mapping and sweeping operations. The number of the mesh in the computational domain of the 2D problem is 63,000. We give an example of the mesh representation of the result of Figure 6i in Figure 8. At the same time, the difference of shapes corresponding to different objective functions can be clearly seen from the mesh representation. Figure 8a,b correspond to objective functions J_1 and J_2, respectively.

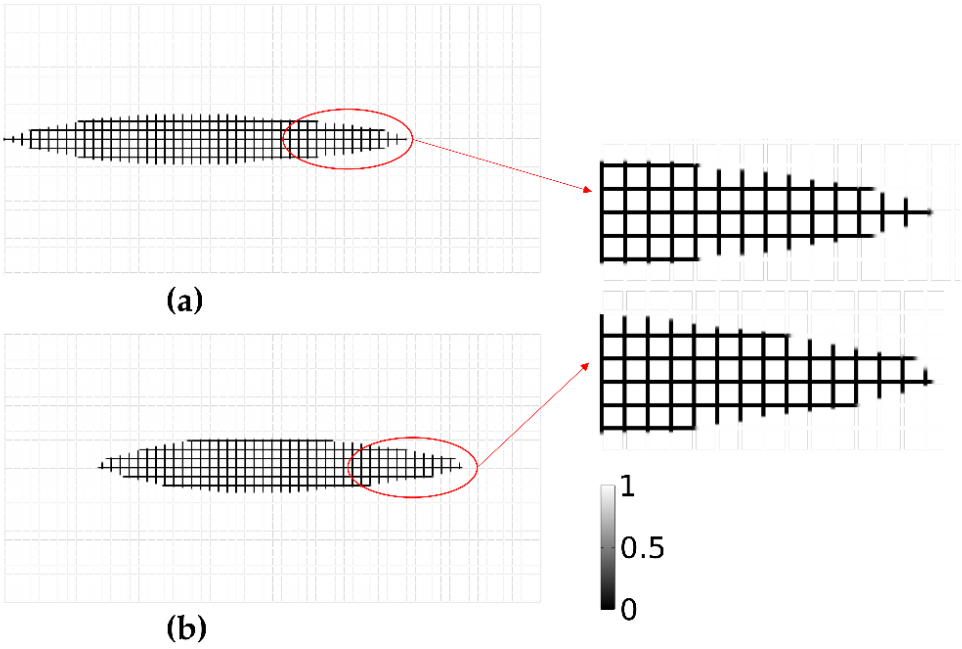

Figure 8. The mesh representation of the result in Figure 6i. (**a**,**b**) respectively show the mesh representation and local enlarged view of the structures corresponding to J_1 and J_2 when the Reynolds number is 500.

4.2. Three-Dimensional Examples

We also study the 3D topology optimization problem of an axisymmetric object with minimum drag in a uniform flow, which takes longer to solve compared with the 2D problem.

Figure 9 shows the modeling and definitive solution conditions of the 3D problem. The pink area is the design domain, and the gray area is the flow domain. The purple one is the structure that we solved. The boundary and initial value conditions of 3D model are similar to the setting of the 2D problem. The length, width, and height of flow domain and design domain are 5L, 2L, 2L, and 3L, 1L, 1L, respectively. The pressure on the outlet surface is zero, and the velocity of the remaining surfaces is U = 1 in the X-direction. Except where noted, the resulting 3D topology optimizations are the same modeling and the same meshing. Of course, other factors such as boundary conditions and initial conditions are the same. Therefore, the settings of each topology structure are not explained one by one.

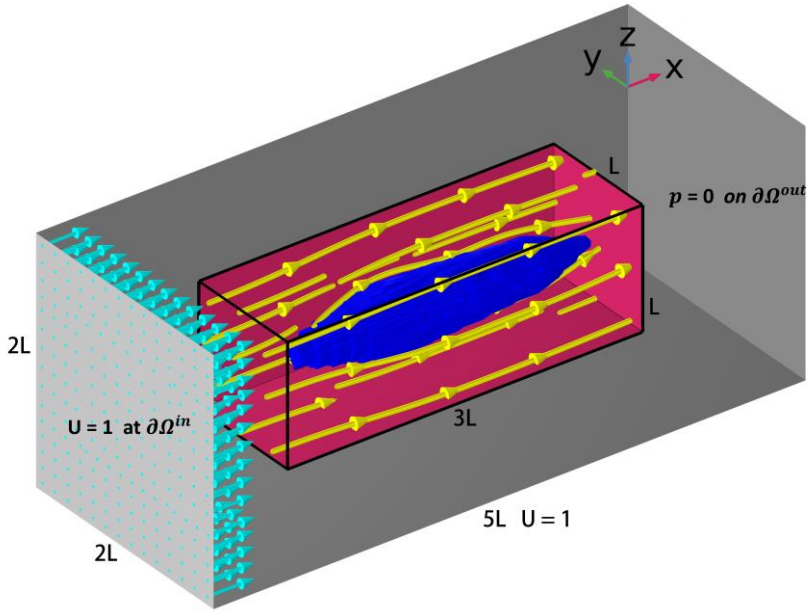

Figure 9. Schematic of the 3D modelling for drag reduction problem.

The optimization body shapes at various Reynolds numbers are governed by objective function J_1 shown in Figure 10. The 3D topology optimization is a standard ellipsoid with Re = 0. When Reynolds number tends to zero, it expresses a state that the inertia force is infinitesimal and can be ignored and there is hardly any memory of the flow state of the previous moment. We express it as Re = 0 for convenience. The structures are similar for Re of 1 and 25, whose shapes are pointed cone-shaped at the head, with a gradually narrowing column from the middle section to the tail section, and a concave area at the tail. As the Reynolds number continues to increase from 50 to 500, the 3D body shapes present a change approximated with the 2D results, with the body shape growing laterally and narrowing, and the head and the tail parts becoming pointed. The overall shape appears to be a spindle-shaped column with the wide middle and narrow ends. This kind of rotating body with a nearly circular cross-section conforms to a streamlined body shape. The standard rotation body obtained is related to the implemented condition with velocity only in the X-direction.

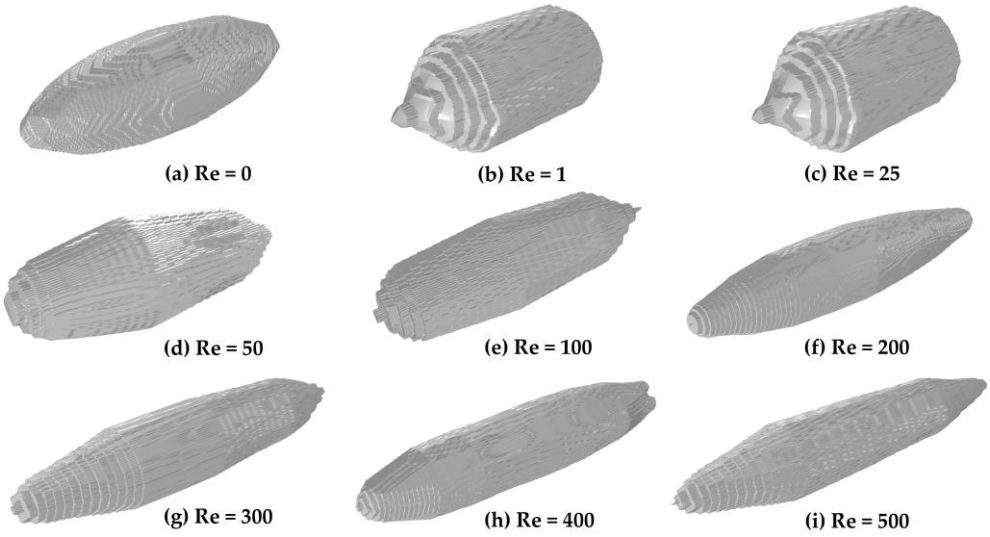

Figure 10. Three-dimensional optimal body shapes for drag reduction corresponding to J_1 at various Reynolds numbers.

The convergence history on the result in Figure 10a is given in Figure 11 including the evolution of the material density. Similarly, the convergence history for the result in the Figure 10f is given in Figure 12.

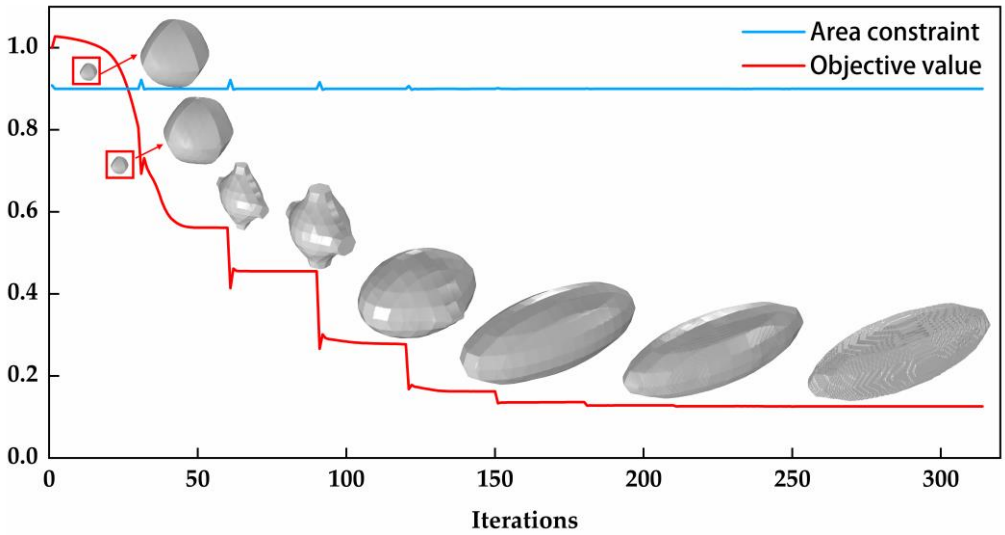

Figure 11. Convergence performance of topology optimization for drag reduction on the body structure in Figure 10a.

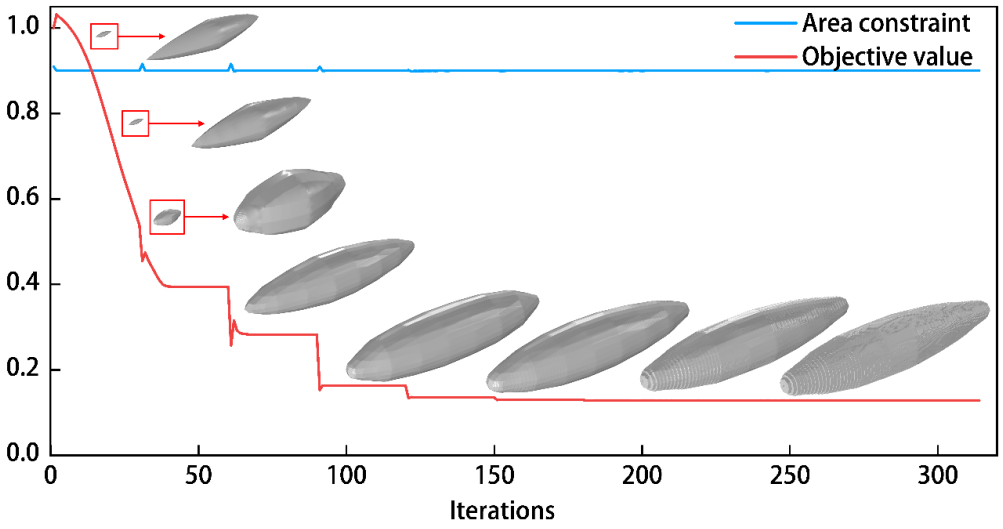

Figure 12. Convergence performance of topology optimization for drag reduction on the body structure in Figure 10f.

It is worth mentioning that the surface smoothness of the body shape is correlated with the mesh density. The surface of the structure generated by the finite element method presents a sawtooth or stepped shape, but with the gradual increase of the mesh density, the surface of the structure will become smooth. As the number of iterations increases, there will also be more details such as the undulations and textures presented on the structural surface. Of course, these are the characteristics of the structure itself, independent of smoothness or roughness. When the mesh density is sufficiently fine, we can clearly see the changes of the entire surface. As shown in Table 1, the mesh density in the appropriate range does not affect the drag results. At the same time, the higher the mesh density, the longer the calculation time. In order to give consideration to the accuracy of results and computational efficiency, the mesh density of the 3D model is selected as 10. The number of the mesh in the computational domain of the 3D problem is 36,000. Therefore, the results

we have obtained so far do not affect the exploration of the relevant regularity. We give an example of the mesh representation of the result of Figure 10a in Figure 13.

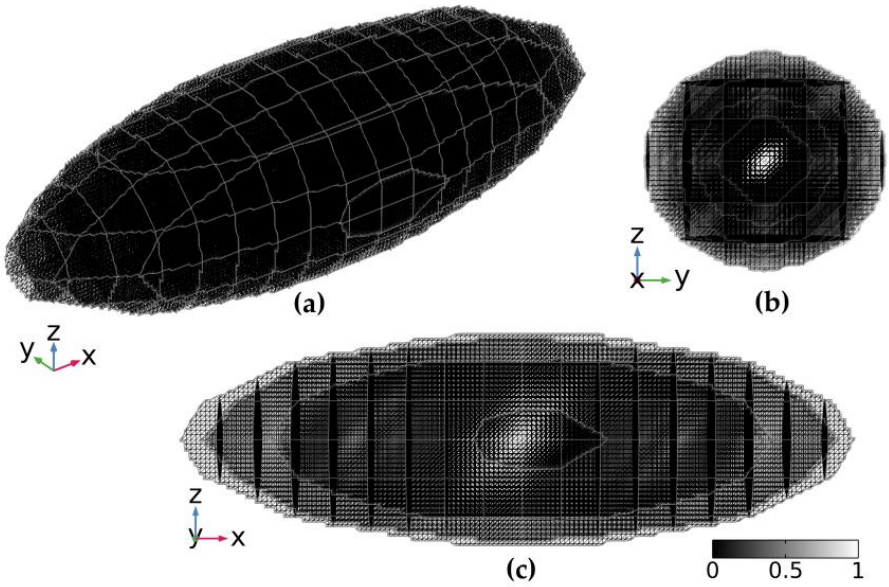

Figure 13. The mesh representation of the result in Figure 10a. (**a**–**c**) show the mesh representation of the structures corresponding to J_1 when Reynolds number is 0 from different perspectives.

In addition, we also investigated the 3D body shape governed by J_2, whose integrand contains a convection term. Because the body shape corresponding to the larger Reynolds number has the solid material close to the design domain during the iterative evolution process, we set the area fraction to 0.98 to ensure that the complete body shape is obtained. Shown in Figure 14, the overall structure is a similar cylinder with a diameter change in the cross-section from head to tail. For this group of structures, the front section is conical, and the mid-section cylinder gradually thickens until the tail rapidly narrows, with the Reynolds numbers from 0 to 500. When Reynolds number is below 300, the front sections are similar, and up to 300 the head regions become blunt. In fact, the structure cannot be regarded as a standard rotating body because the cross-section of the structure contains ellipse and circle shapes with different Reynolds numbers, as shown in Figure 15.

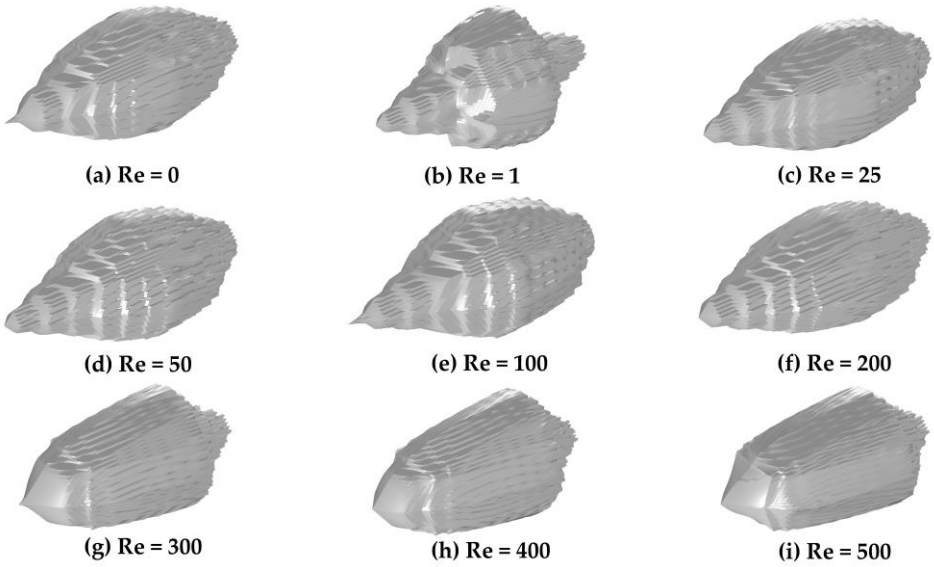

Figure 14. 3D optimal body shapes for drag reduction corresponding to J_2 at various Reynolds numbers.

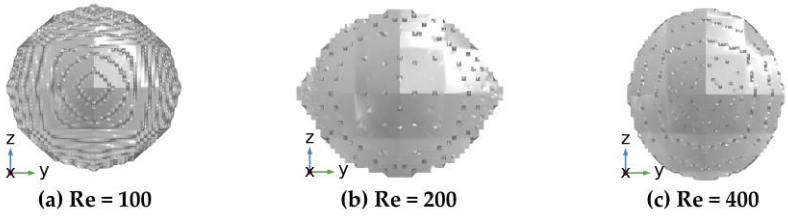

Figure 15. Rear view of some structures in Figure 14.

It is not difficult to see that there is a big difference in the structure of objective function J_1 and J_2 in three-dimensional problems. Compared with the body shapes in Figure 10, this group of structures seems to be covered with a thick shell in the middle of the spindle cylinder, which is particularly evident from the structure corresponding to Re = 1 in Figure 14b. We guess that the effect of convection term may widen the middle of the structure in this problem. In order to verify this idea and make the result more obvious, we purposely remove the Z-axis component of the convection term in J_2 and obtain the following results in Figure 16. It is obvious from Figure 16b,c that with Y-axis component of the convection term, the Y-direction of body is wider. Without Z-axis component of the convection term, there is no material growth in the central main part in the Z- direction. In addition, the convection effect enhances with the increase of the Reynolds number. Therefore, when the Reynolds number is less than 200, the shape changes little, while when it is greater than 300, the effect is obvious.

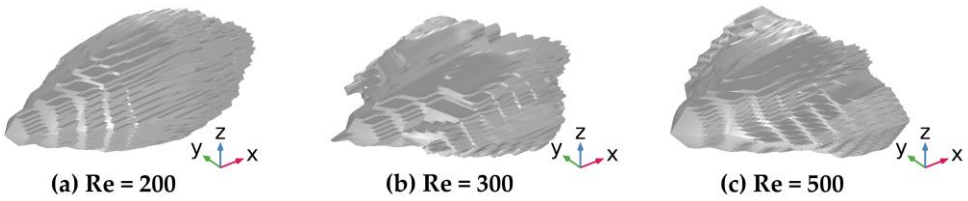

Figure 16. New body shapes correspond to some structures in Figure 14 after removing the Z-axis component of the convection term.

Compared with the structures of Figure 10, the structures in Figure 14 have more obvious oscillating in the convergence history with the appearance of sharp corners. The convergence performance corresponding to Reynolds numbers 0 and 200 is shown in Figures 17 and 18, respectively.

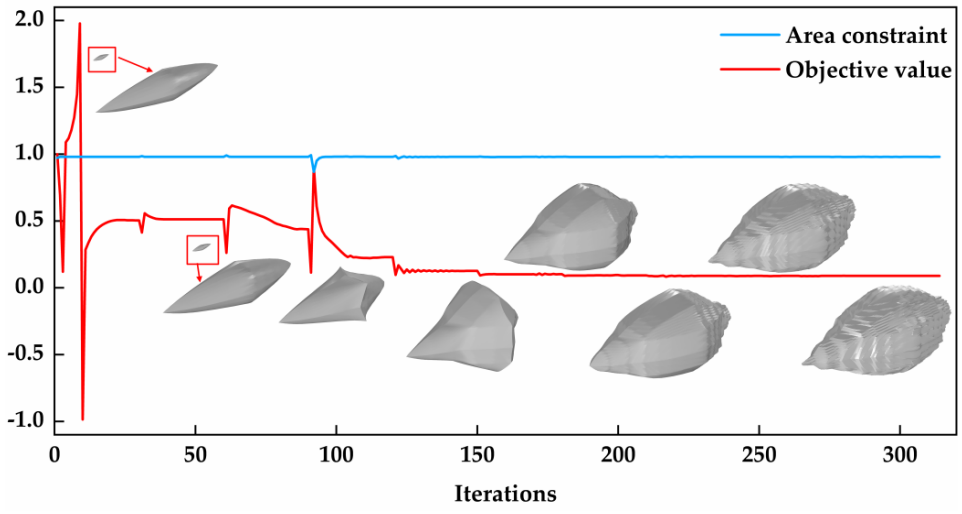

Figure 17. Convergence performance of topology optimization for drag reduction on the body structure in Figure 10a.

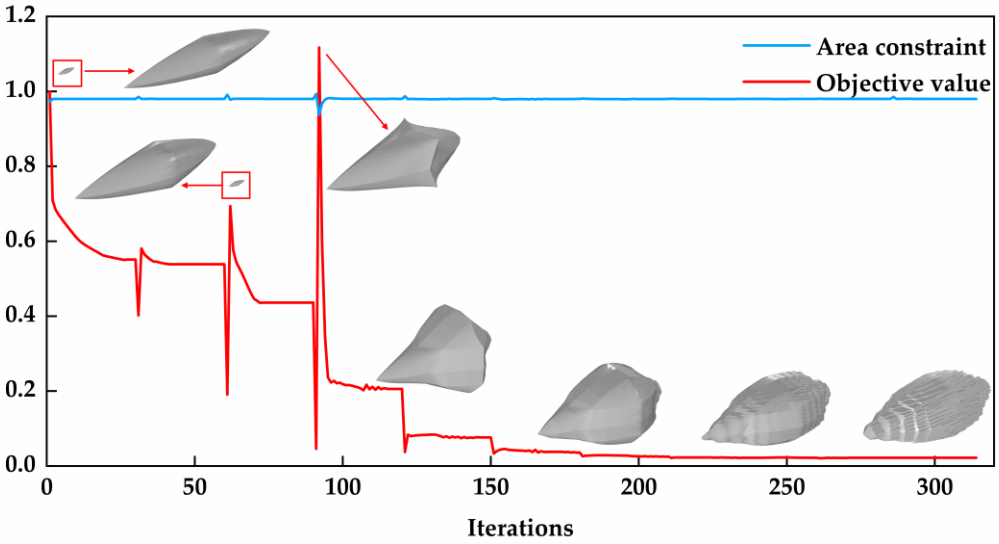

Figure 18. Convergence performance of topology optimization for drag reduction on the body structure in Figure 10f.

In addition, the mesh representation of the result in Figure 14a is shown in Figure 19. We can intuitively see the characteristics of the structure surface from the mesh representation. Like the curvature variation of the surface, it is a property of the structure itself, independent of the mesh density. However, the mesh density affects the smoothness or roughness of the structure surface using the finite method. The higher the mesh density, or the smaller the filtering radius, the smoother the jagged and stepped shapes in the structure surface. We use the fixed mesh achieved by mapping and sweeping operations. The number of the mesh in the computational domain of the 3D problem is 63,000.

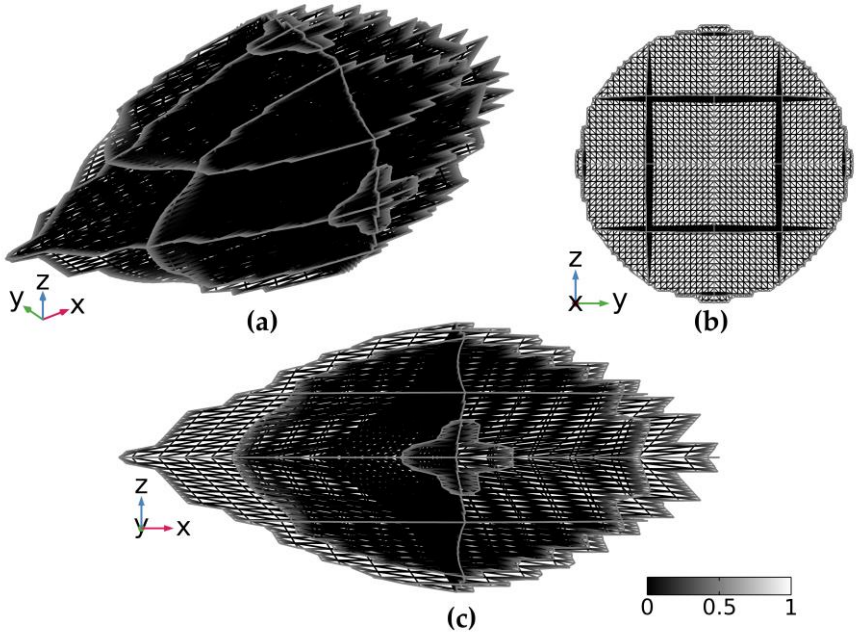

Figure 19. The mesh representation of the result in Figure 14a. (**a**–**c**) show the mesh representation of the structures corresponding to J_2 when Reynolds number is 0 from different perspectives.

Next, we compare the change of drag value with Reynolds number between the two objective functions J_1 and J_2. Since the results obtained from the two objective functions are using different area fractions, in order to compare at the same conditions and take into account the rapidity of calculation, we reduce the design domain and flow domain of the

3D model by 5 times; set the area fraction to 0.9; and obtain the change of the drag values with the Reynolds number corresponding to the two objective functions, as shown in the Figure 20.

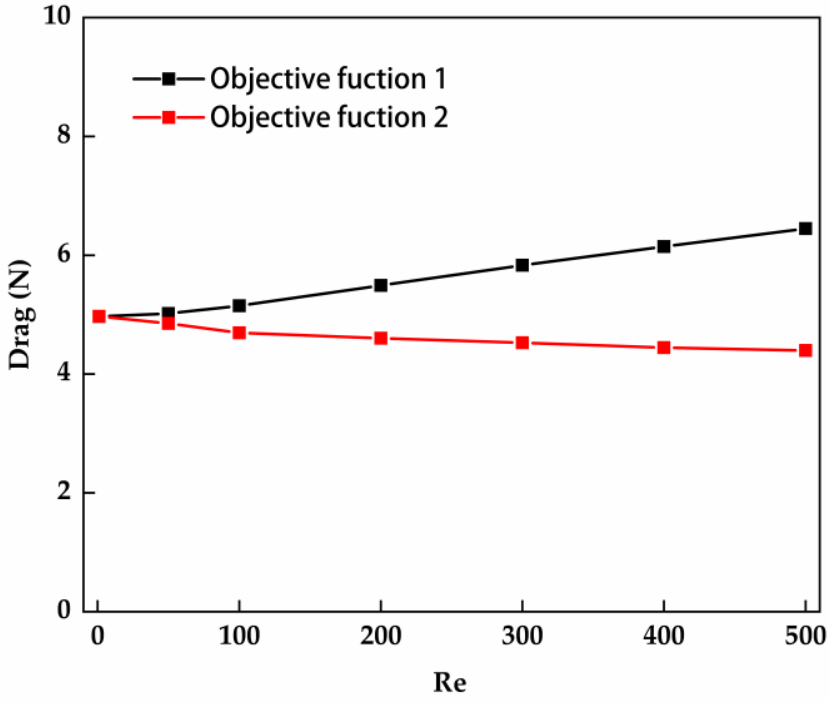

Figure 20. Comparison of the drag values for two objective functions at different Reynolds numbers in 3D problem.

In the 2D problems, the drag values corresponding to the two objective functions are positively correlated with the Reynolds number. Obviously, the law of variation of drag with the Reynolds number corresponding to objective function 2 in 3D problem is unexpected, but the law obtained after changing the size of the design domain and the area fraction is consistent with this. The only difference between the two results is the existence or not of a convection term in the objective function. Therefore, it can be inferred that with the increase of Reynolds number, the drag reduction effect of convection term will increase in the currently set model. As for the reason, although it has not been confirmed, we guess it is because considering the convection term, the pressure difference near the structure surface leads to the change of velocity, and finally affects the drag.

4.3. Field Characteristics

Here, we will discuss the effect of body shape on the drag reduction from the distribution of pressure and the change of flow field.

The pressure contour distribution on the surfaces of the 2D body shapes are shown in Figure 21. At ultra-low Reynolds numbers such as Re = 1, the pressure distribution along the structure is as follows: the maximum positive value appears near the tip of the head; gradually the pressure value decreases toward the direction of the tail until a certain point, then becomes negative increasing in the opposite direction; and the maximum negative pressure appears in the tail. With the increase of the Reynolds number, the pressure on the structure increases, the position of the maximum positive pressure contour changes little, and the maximum negative pressure contour gradually extends from the tail forward. In other words, the position of the point experiencing the shift from positive to negative pressure value gradually moves toward the front of the structure with the increase of the Reynolds number.

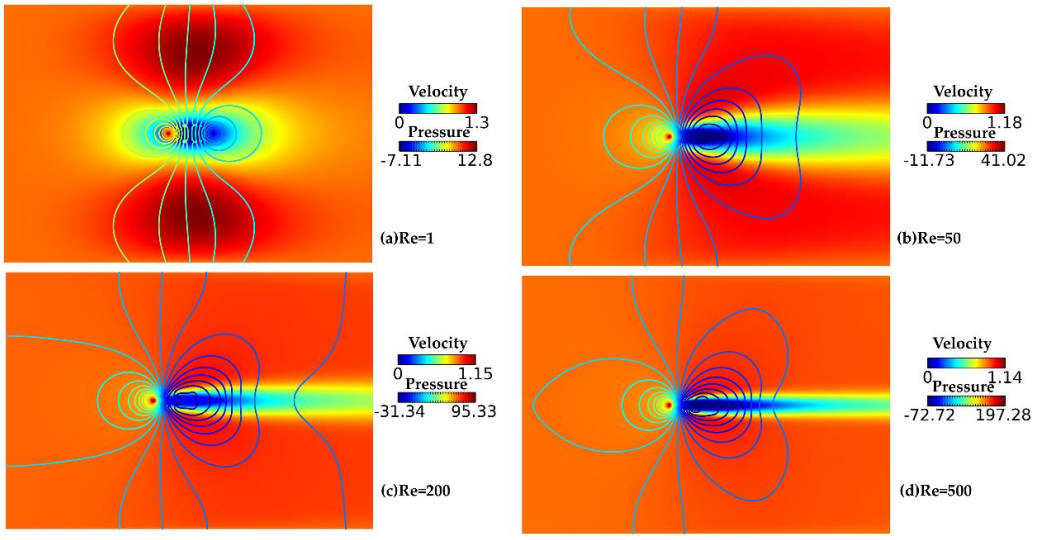

Figure 21. Velocity field and pressure contours in the flow domain for 2D structures of objective function J_1. In the above illustrations from (**a**–**d**), the upper legend corresponds to fluid velocity and the lower one corresponds to fluid pressure contours.

Regarding the change of pressure with the Reynolds number, it is more intuitive to observe from the pressure iso-surface of the 3D body shapes, in Figure 22. At the same time, it is observed that the pressure gradient on the 3D structural surface has the alternating change process of the positive gradient and negative gradient along the direction of fluid travel (X-direction). In addition, at each interval of the favorable or adverse pressure gradient, the pressure gradient decreases follow the direction of the outer normal of the wall. The largest and second largest positive pressure gradients occur in the flow field near the head and tail of the structure, while the maximum value section of the negative pressure gradient gradually moves from the tail cusp along the X-axis direction to the shoulder of the structure as the Reynolds number increases from 0 to 500.

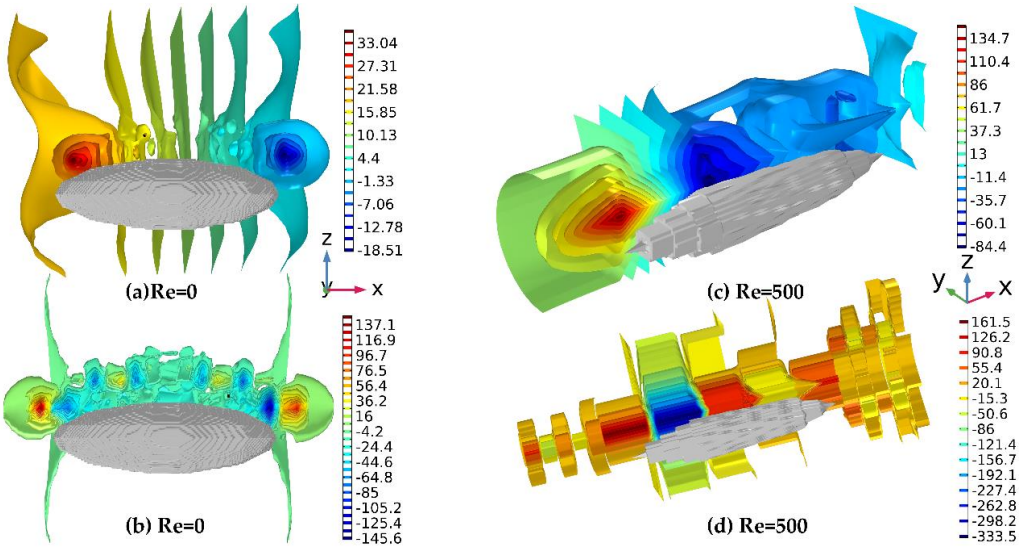

Figure 22. Isobaric surfaces and isobaric gradient surfaces for X–axis direction in the flow domain containing 3D structures of objective function J_1.

However, there are some differences of pressure field distribution between objective function 1 and 2. As shown in Figure 23, with the increase of the Reynolds number, the pressure position corresponding to the maximum negative value changes little; at the

same time, the alternating frequency of positive and negative pressure gradient along the direction of fluid travel is not high.

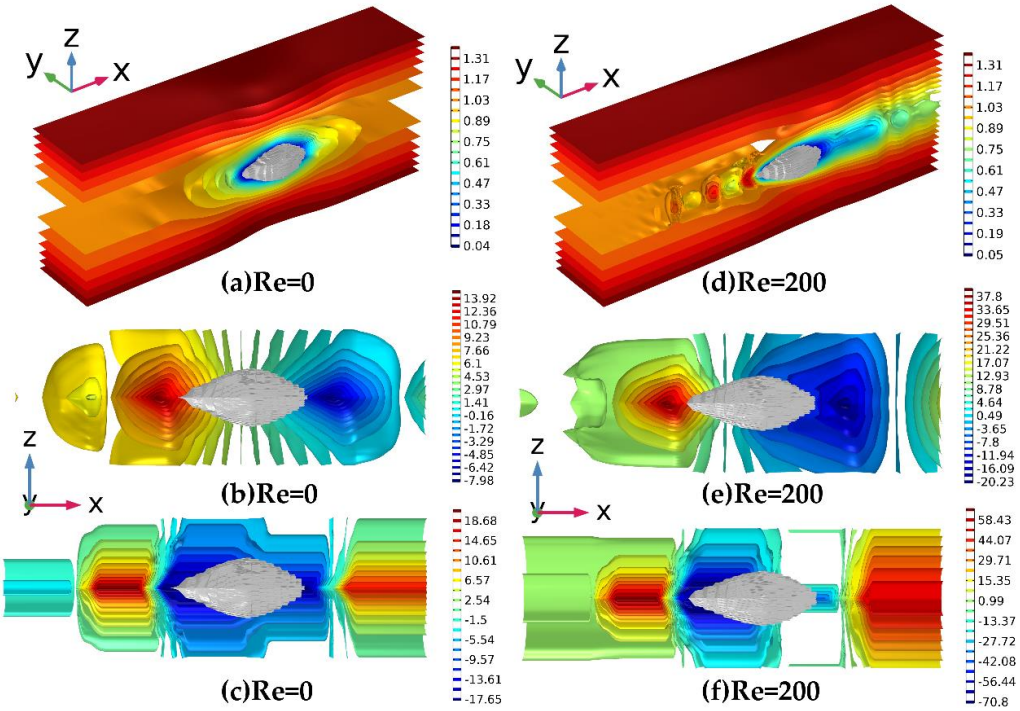

Figure 23. Isobaric surfaces and isobaric gradient surfaces for X–axis direction in the flow domain containing 3D structures of objective function J_2.

The boundary layer and its interaction with nearby pressure gradients play a major role in influencing body surface flow. We can know that when the fluid just touches the curve surface of the structure, the fluid velocity increases, and the fluid pressure decreases accompanied by a favorable pressure gradient (negative); beyond a certain point, near the shoulder at Re = 500, however, the force due to pressure differences changes sign from being an accelerating force to being a retarding force. In response, the velocity begins to decrease, and the pressure increases with an adverse pressure gradient (positive). Although flow near the wall of the structure slows down approaching stopping, with frictional drag approaching zero and the pressure drag still existing, there is no boundary layer separation, which proves that the structures obtained by topology optimization methods are well streamlined. The obvious evidence that no flow separation occurs is that the velocity around the structure, although reduced, is positive from Figure 17. In fact, this can be seen more intuitively in the velocity field of the flow field in Figure 23a,d.

Although we use the integral method to find drag through the momentum equation without distinguishing frictional drag and pressure drag, it is necessary to distinguish the two forms of drag in order to explore the mechanism of drag for different flow phenomena. The magnitude of frictional drag and pressure drag depends on the geometry of the object relative to the flow direction. When drag is dominated by frictional drag in the absence of an angle of attack, we say the body is streamlined, and when it is dominated by pressure drag, we say the body is bluff. When streamlining an object, in order to reduce the total drag, it needs to be balanced in these two aspects. With the increase of the Reynolds number and enhancement of the effect of convection term, the shape with the minimal total drag is not necessarily the most streamlined shape.

5. Conclusions

This article has developed a topology optimization approach of variable density for shape design in steady incompressible fluid. We also give the two expressions of the

drag force on the implicit interface of the structure and compare them through numerical examples. The presented topology optimization approach is used to study the optimal shape of drag reduction at the low Reynolds numbers. We have obtained the topology optimization structure with minimum drag as the objective function in 2D and 3D cases. In general, the drag is positively correlated with Reynolds number and the proportion of solid materials; in the 2D cases, the aspect ratio of the structure corresponding to the objective function with convection term is smaller, and the drag value is also relatively small; in the 3D cases, there is an unexpected law of variation of drag with the Reynolds number due to the effect of convection term and we give some conjectures. In addition, we analyze the distribution and the change of velocity, pressure, and pressure gradient on the surface of the structures to explore the law of fluid motion, and thus obtain some conclusions about the drag. At the same time, we prove that the 3D structures we obtained are well streamlined.

The method we outline may give a potential design idea for body shape drag reduction of micro underwater vehicles and other underwater equipment worked in low speed. In the future, we will consider the drag reduction configurations in more conditions, including the attack angle and lift constraints, and may also conduct research in a larger range of Reynolds numbers. Meanwhile, we will process and fabricate the topological results obtained so that the calculated values can be compared with the experimental ones.

Author Contributions: Conceptualization, Y.D.; methodology, N.Z.; software, Y.D.; validation, N.Z.; formal analysis, N.Z.; investigation, N.Z.; resources, J.Z., H.H. and Y.M.; data curation, N.Z.; writing—original draft preparation, N.Z.; writing—review and editing, J.Z., H.H. and Y.M.; visualization, N.Z.; supervision, Y.D.; funding acquisition, Y.D. All authors have read and agreed to the published version of the manuscript.

Funding: The authors acknowledge the support of the CAS Project for Young Scientists in Basic Research (No. YSBR-066).

Institutional Review Board Statement: The article does not contain any studies with human participants or animals performed by any of the authors.

Informed Consent Statement: Not applicable.

Data Availability Statement: The authors state that all the data necessary to replicate the results are presented in the manuscript. Relevant parts of the code can be shared upon contacting the corresponding author.

Acknowledgments: The authors are grateful to K. Svanberg of KTH for supplying the codes of the method of moving asymptotes. They are also grateful to the reviewers' kind attention and valuable suggestions.

Conflicts of Interest: On behalf of all of the authors, the corresponding author states that there are no conflict of interest.

References

1. Busch, J.; Barthlott, W.; Brede, M.; Terlau, W.; Mail, M. Bionics and Green Technology in Maritime Shipping: An Assessment of the Effect of Salvinia Air-Layer Hull Coatings for Drag and Fuel Reduction. *Philos. Trans. R. Soc. A* **2019**, *377*, 20180263. [CrossRef] [PubMed]
2. Zhang, X.; Yu, Y. Analysis of the Propulsion Performance and Internal Flow Field of an Underwater Launcher. *Appl. Sci.* **2022**, *12*, 5443. [CrossRef]
3. Chen, G.; Sun, T.; Yang, S.; Miao, Z.; Tan, H. A Study on the Cavitating Flow around an Elliptical Disk-Shaped Cavitator for Non-Body-of-Revolution Underwater Vehicles. *Eng. Appl. Comput. Fluid Mech.* **2023**, *17*, 2159882. [CrossRef]
4. Wu, T.; Chen, W.; Zhao, A.; He, P.; Chen, H. A Comprehensive Investigation on Micro-Structured Surfaces for Underwater Drag Reduction. *Ocean. Eng.* **2020**, *218*, 107902. [CrossRef]
5. Feng, X.; Sun, P.; Tian, G. Recent Developments of Superhydrophobic Surfaces (SHS) for Underwater Drag Reduction Opportunities and Challenges. *Adv. Mater. Inter* **2022**, *9*, 2101616. [CrossRef]
6. Alijani, M.; Zeinali, M.; Nouri, N.M. Designing of the Body Shape of an Autonomous Underwater Vehicle Using the Design of Experiments Method. *Proc. Inst. Mech. Eng. Part C J. Mech. Eng. Sci.* **2019**, *233*, 6307–6325. [CrossRef]

7. Salinas, M.F.; Botez, R.M.; Gauthier, G. New Validation Methodology of an Adaptive Wing for UAV S45 for Fuel Reduction and Climate Improvement. *Appl. Sci.* **2023**, *13*, 1799. [CrossRef]
8. Hamed, A. Multi-Objective Optimization Method of Trimaran Hull Form for Drag Reduction and Propeller Intake Flow Improvement. *Ocean. Eng.* **2022**, *244*, 110352. [CrossRef]
9. Ignacio, L.C.; Victor, R.R.; Francisco, D.R.R.; Pascoal, A. Optimized Design of an Autonomous Underwater Vehicle, for Exploration in the Caribbean Sea. *Ocean. Eng.* **2019**, *187*, 106184. [CrossRef]
10. Saghafi, M.; Lavimi, R. Optimal Design of Nose and Tail of an Autonomous Underwater Vehicle Hull to Reduce Drag Force Using Numerical Simulation. *Proc. Inst. Mech. Eng. Part M J. Eng. Marit. Environ.* **2020**, *234*, 76–88. [CrossRef]
11. Bianchi, G.; Cinquemani, S.; Resta, F. Bio-inspired design of an underwater robot exploiting fin undulation propulsion. *Appl. Sci.* **2021**, *11*, 2556. [CrossRef]
12. Zhou, H.; Feng, B.; Liu, Z.; Chang, H.; Cheng, X. NURBS-Based Parametric Design for Ship Hull Form. *JMSE* **2022**, *10*, 686. [CrossRef]
13. Bendsøe, M.P.; Sigmund, O. *Topology Optimization: Theory, Methods, and Applications*; Springer Science & Business Media: Berlin, Germany, 2003.
14. Zhan, T. Progress on Different Topology Optimization Approaches and Optimization for Additive Manufacturing: A Review. *J. Phys. Conf. Ser.* **2021**, *1939*, 012101. [CrossRef]
15. Zhu, J.; Zhou, H.; Wang, C.; Zhou, L.; Yuan, S.; Zhang, W. A Review of Topology Optimization for Additive Manufacturing: Status and Challenges. *Chin. J. Aeronaut.* **2021**, *34*, 91–110. [CrossRef]
16. Garrett, C.A.B. LVII. On the Lateral Vibration of Bars. *Lond. Edinb. Dublin Philos. Mag. J. Sci.* **1904**, *8*, 581–589. [CrossRef]
17. Bendsøe, M.P.; Kikuchi, N. Generating Optimal Topologies in Structural Design Using a Homogenization Method. *Comput. Methods Appl. Mech. Eng.* **1988**, *71*, 197–224. [CrossRef]
18. Xie, Y.M.; Steven, G.P. A Simple Evolutionary Procedure for Structural Optimization. *Comput. Struct.* **1993**, *49*, 885–896. [CrossRef]
19. Bendsøe, M.P.; Sigmund, O. Material Interpolation Schemes in Topology Optimization. *Arch. Appl. Mech. (Ing. Arch.)* **1999**, *69*, 635–654. [CrossRef]
20. Wang, M.Y.; Wang, X.; Guo, D. A Level Set Method for Structural Topology Optimization. *Comput. Methods Appl. Mech. Eng.* **2003**, *192*, 227–246. [CrossRef]
21. Deaton, J.D.; Grandhi, R.V. A Survey of Structural and Multidisciplinary Continuum Topology Optimization: Post 2000. *Struct. Multidisc. Optim.* **2014**, *49*, 1–38. [CrossRef]
22. Sigmund, O.; Maute, K. Topology Optimization Approaches: A Comparative Review. *Struct. Multidisc. Optim.* **2013**, *48*, 1031–1055. [CrossRef]
23. Papoutsis-Kiachagias, E.M.; Giannakoglou, K.C. Continuous Adjoint Methods for Turbulent Flows, Applied to Shape and Topology Optimization: Industrial Applications. *Arch. Computat. Methods Eng.* **2016**, *23*, 255–299. [CrossRef]
24. Gao, J.; Xiao, M.; Zhang, Y.; Gao, L. A Comprehensive Review of Isogeometric Topology Optimization: Methods, Applications and Prospects. *Chin. J. Mech. Eng.* **2020**, *33*, 87. [CrossRef]
25. Wu, J.; Sigmund, O.; Groen, J.P. Topology Optimization of Multi-Scale Structures: A Review. *Struct. Multidisc. Optim.* **2021**, *63*, 1455–1480. [CrossRef]
26. Alexandersen, J.; Andreasen, C.S. A Review of Topology Optimisation for Fluid-Based Problems. *Fluids* **2020**, *5*, 29. [CrossRef]
27. Pironneau, O. On Optimum Profiles in Stokes Flow. *J. Fluid Mech.* **1973**, *59*, 117–128. [CrossRef]
28. John, V. Higher Order Ÿnite Element Methods and Multigrid Solvers in a Benchmark Problem for the 3D Navier–Stokes Equations. *Int. J. Numer. Methods Fluids* **2002**, *40*, 775–798. [CrossRef]
29. John, V. Reference values for drag and lift of a two-dimensional time-dependent flow around a cylinder. *Int. J. Numer. Methods Fluids* **2004**, *44*, 777–788. [CrossRef]
30. Mohammadi, B.; Pironneau, O. Shape Optimization in Fluid Mechanics. *Annu. Rev. Fluid Mech.* **2004**, *36*, 255–279. [CrossRef]
31. Dapogny, C.; Frey, P.; Omnès, F.; Privat, Y. Geometrical Shape Optimization in Fluid Mechanics Using FreeFem++. *Struct. Multidisc. Optim.* **2018**, *58*, 2761–2788. [CrossRef]
32. Brandenburg, C.; Lindemann, F.; Ulbrich, M.; Ulbrich, S. A Continuous Adjoint Approach to Shape Optimization for Navier Stokes Flow. In *Optimal Control of Coupled Systems of Partial Differential Equations*; Kunisch, K., Sprekels, J., Leugering, G., Tröltzsch, F., Eds.; International Series of Numerical Mathematics; Birkhäuser Basel: Basel, Switzerland, 2009; Volume 158, pp. 35–56, ISBN 978-3-7643-8922-2.
33. Shi, L.; Yang, G.; Yao, S. Large Eddy Simulation of Flow Past a Square Cylinder with Rounded Leading Corners: A Comparison of 2D and 3D Approaches. *J. Mech. Sci. Technol.* **2018**, *32*, 2671–2680. [CrossRef]
34. Cravero, C.; Marogna, N.; Marsano, D. A Numerical Study of Correlation Between Recirculation Length and Shedding Frequency in Vortex Shedding Phenomena. *Wseas Trans. Fluid Mech.* **2021**, *16*, 48–62. [CrossRef]
35. Xia, L.; Zou, Z.-J.; Wang, Z.-H.; Zou, L.; Gao, H. Surrogate Model Based Uncertainty Quantification of CFD Simulations of the Viscous Flow around a Ship Advancing in Shallow Water. *Ocean. Eng.* **2021**, *234*, 109206. [CrossRef]
36. Cravero, C.; De Domenico, D.; Marsano, D. The Use of Uncertainty Quantification and Numerical Optimization to Support the Design and Operation Management of Air-Staging Gas Recirculation Strategies in Glass Furnaces. *Fluids* **2023**, *8*, 76. [CrossRef]
37. Borrvall, T.; Petersson, J. Topology Optimization of Fluids in Stokes Flow. *Int. J. Numer. Meth. Fluids* **2003**, *41*, 77–107. [CrossRef]

38. Gersborg-Hansen, A.; Bendsøe, M.P.; Sigmund, O. Topology Optimization Using the Finite Volume Method. *Struct. Multidiscipl. Optim.* **2005**, *50*, 523–535.
39. Deng, Y.; Liu, Z.; Zhang, P.; Liu, Y.; Wu, Y. Topology Optimization of Unsteady Incompressible Navier–Stokes Flows. *J. Comput. Phys.* **2011**, *230*, 6688–6708. [CrossRef]
40. Alexandersen, J. A Detailed Introduction to Density-Based Topology Optimisation of Fluid Flow Problems with Implementation in MATLAB. *Struct. Multidisc. Optim.* **2023**, *66*, 12. [CrossRef]
41. Lazarov, B.S.; Sigmund, O. Filters in Topology Optimization Based on Helmholtz-Type Differential Equations. *Int. J. Numer. Meth. Engng.* **2011**, *86*, 765–781. [CrossRef]
42. Wang, F.; Lazarov, B.S.; Sigmund, O. On Projection Methods, Convergence and Robust Formulations in Topology Optimization. *Struct. Multidisc. Optim.* **2011**, *43*, 767–784. [CrossRef]
43. Guest, J.K.; Prévost, J.H.; Belytschko, T. Achieving Minimum Length Scale in Topology Optimization Using Nodal Design Variables and Projection Functions. *Int. J. Numer. Methods Eng.* **2004**, *61*, 238–254. [CrossRef]
44. Deng, Y.; Liu, Z.; Korvink, J.G. Topology Optimization on Two-Dimensional Manifolds. *Comput. Methods Appl. Mech. Eng.* **2020**, *364*, 112937. [CrossRef]
45. Kristian, B.; Clason, C.; Kunisch, K.; Winckel, G. (Eds.) *Control and Optimization with PDE Constraints*; Springer: Basel, Switzerland, 2013; Volume 164, ISBN 978-3-0348-0630-5.
46. Deng, Y.; Zhang, W.; Liu, Z.; Zhu, J.; Korvink, J.G. Topology Optimization for Surface Flows. *J. Comput. Phys.* **2022**, *467*, 111415. [CrossRef]
47. Dziuk, G.; Elliott, C.M. Finite Element Methods for Surface PDEs. *Acta Numer.* **2013**, *22*, 289–396. [CrossRef]
48. Svanberg, K. The Method of Moving Asymptotes—A New Method for Structural Optimization. *Int. J. Numer. Methods Eng.* **1987**, *24*, 359–373. [CrossRef]
49. Sigmund, O. Morphology-Based Black and White Filters for Topology Optimization. *Struct. Multidisc. Optim.* **2007**, *33*, 401–424. [CrossRef]
50. Kondoh, T.; Matsumori, T.; Kawamoto, A. Drag Minimization and Lift Maximization in Laminar Flows via Topology Optimization Employing Simple Objective Function Expressions Based on Body Force Integration. *Struct. Multidisc. Optim.* **2012**, *45*, 693–701. [CrossRef]
51. Wo, M.S.; Gobithaasan, R.U.; Miura, K.T.; Loy, K.C.; Harun, F.N. Analysis of Drag Coefficients around Objects Created Using Log-Aesthetic Curves. *Mathematics* **2022**, *11*, 103. [CrossRef]
52. Garcke, H.; Hecht, C.; Hinze, M. Numerical approximation of phase field based shape and topology optimization for fluids. *SIAM J. Sci. Comput.* **2015**, *37*, A1846–A1871. [CrossRef]